Theory of strong-field sequential double ionization of polyatomic molecules

C. H. Yuen [*] and C. D. Lin [†]

J. R. Macdonald Laboratory, Department of Physics, Kansas State University, Manhattan, Kansas 66506, USA

Understanding of strong-field sequential double ionization (SDI) of molecules by a highly intense infrared laser pulse could be the key to observing electron motion in molecules in the attosecond to femtosecond timescale. Based on a novel density matrix approach for SDI (DM-SDI), a recent theoretical study [Yuen and Lin, Phys. Rev. A **109**, L011101 (2024)] has shown that SDI can be used as a probe to monitor the changes in vibronic coherence in homonuclear diatomic molecules. In this article, we extend the DM-SDI model to general molecules that could possess permanent dipole moments and arbitrary symmetry. We apply the model to SDI of a water molecule and identify the formation pathway of individual dication states. We further deduce that kinetic energy release spectra from two- and three-body fragments could carry the signature of vibronic coherence between the lowest two states of the water cation. Our results suggest that observables from the SDI probe can be interpreted intuitively with only the knowledge of electronic structures of populated ionic states, making the SDI probe to be a highly desirable probing scheme for vibronic coherence in generic molecules.

I. INTRODUCTION

Strong-field sequential double ionization (SDI) is a promising but unexpected process to probe vibronic coherence in molecules. Strong-field SDI of molecules has been studied experimentally since the early 2000s [1]. By illuminating a highly intense infrared (IR) laser pulse on neutral molecules, the neutral could undergo tunnel ionization twice and dissociative dications could be formed, resulting in two or more molecular fragments. With the emergence of coincidence measurement techniques such as the velocity map imaging [2] or COLTRIMS [3,4], momenta and kinetic energy release of the ionic fragments from SDI of different molecules have been investigated over the years [5–18]. On the other hand, electronic coherence is created by pumping a molecule into a superposition of electronic states. Since nuclei move differently on different potential energy surfaces, electronic coherence is then influenced by the femtosecond (fs) nuclear motion. We refer to such varying coherence as vibronic coherence. Survival of the vibronic coherence could result in periodic charge migration across the molecular skeleton [19,20], while decoherence could result in charge transfer within the molecule. Therefore, observing and manipulating vibronic coherence in the femtosecond to attosecond timescale is the frontier of ultrafast science [21–23], holding the keys to exert unprecedented control over chemical reactions [24–26]. SDI of molecules and vibronic coherence—two seemingly unrelated topics—have recently been found to be connected, in which the former can be used to probe the changes in the latter, thanks to the recent theoretical development on SDI of molecules [27–29].

SDI of molecules is notoriously difficult to model using first-principles approaches. To resolve the yield of different

dication states, the final wave function needs to be projected onto double continuum states so that the ionized electrons cannot be neglected. However, due to the large peak laser intensity in the SDI regime, the ionized electrons drift far away from the nuclei, requiring a huge simulation box with expensive computational costs. Furthermore, to compare simulated results directly with experiments, one has to consider many different molecular orientations with respect to the laser polarization, making the simulation even more costly. These challenges have been the major obstacles in modeling SDI of molecules over the years.

Since SDI is driven by the laser field instead of rescattering electrons, it is reasonable to neglect the ionized electrons, resulting in the ion and dication being an open quantum system. Density matrix formalism is then required and the dynamics is governed by the von Neumann-Liouville equation. A significant advantage of the density matrix approach is that many-body electronic wave functions are not directly involved, allowing for efficient computations. Density matrix approaches have been utilized ubiquitously in physical science [30,31]. Early adoption of the density matrix approach in strong-field physics was done by Santra and coworkers [32,33] for single ionization of noble gas atoms. Pfeiffer *et al.* developed a simple density matrix approach to treat SDI of neon and xenon [34]. Zhao and coworkers [35] also employed a density matrix approach to model the lasing of N_2^+, allowing simultaneous description of laser couplings of the ion and tunnel ionization of the neutral. Recently, our group developed a theoretical framework called the density matrix approach for SDI (DM-SDI) [27,28,36]. The DM-SDI model takes advantage of the use of a few-cycle IR pulse, such that the nuclei can be regarded as frozen during the laser interaction. The model can describe the laser couplings and tunnel ionization simultaneously for the neutral, ion, and dication. By considering all possible molecular orientations, the DM-SDI model was benchmarked with the SDI experiments for N_2 [5] and O_2

---
*iyuen@phys.ksu.edu
†cdlin@phys.ksu.edu

[5,37] with excellent agreement on the kinetic energy release (KER) spectra.

From the theoretical studies of SDI of N_2 [27] and O_2 [28], we also found that SDI is partly driven by laser couplings between ionic states. Changes in vibronic coherence between the ionic states will then lead to changes in the strength of laser couplings, therefore changing their transient population [29]. These ionic states are subsequently tunnel ionized to form dications. As a result, changes in the transient ionic population is translated to the dication yields, and the variation of the vibronic coherence is imprinted to SDI observables such as the kinetic energy release spectrum.

With the prospects of using SDI to probe vibronic coherence in molecules [29], it is highly desirable to extend the DM-SDI model for generic molecules, which could possess permanent dipole moments and could be nonlinear. Water molecule is of particular interest since it is a nonlinear molecule with simple electronic structures and nonzero permanent dipole moments. Several aspects of strong-field double ionization of water have been investigated experimentally: Geometry dependence [38,39], ion-electron coincidence [40], nuclear dynamics during [16,17] and after [18] double ionization, and bond rearrangement [11]. Meanwhile, theoretical investigations had been limited to calculating angular dependence of tunnel ionization rate from different orbitals [16,40–43] and to modeling the nuclear dynamics of the water cation [17] and dication [44].

In this article, we develop a comprehensive theory for strong-field SDI of polyatomic molecules. The theory is then used to obtain the yield of relevant water dication states at different molecular orientations. It has been known that the momentum distribution of the water dication fragments in strong-field experiments deviates significantly from that in single-photon double-ionization experiments [45] and field-free trajectory calculations [44]. Therefore, we postpone the mapping of orientation dependence dication yield to experimental observables. By tuning different features of the model, we identify the formation pathway of each dication state, predicting that vibronic coherence between the X^2B_1 and A^2A_1 states of water cation could be observed experimentally in both two-body and three-body KER spectra using the SDI probe. While the B^2B_2 state of water cation is also populated, we predicted that the influence of vibronic coherence between the A^2A_1 and B^2B_2 states on the KER spectra could be too weak to observe, particularly if the carrier envelope phase (CEP) of the IR pulse is not stabilized in each shot.

This article is arranged as follows. In Sec. II, we provide a self-contained description of the theoretical approach and computational details of electronic structures. We discuss the mechanism of SDI of water by performing calculations at different levels of theory in Sec. III. The formation pathway of each dication state is identified and the influence of CEP of the IR pulse on the dication yield is discussed. Finally, we conclude and give an outlook in Sec. IV.

II. THEORETICAL APPROACH

To improve the readability, we divide this section into several subsections. Section II A concerns the conventions used throughout this paper. It should be noted that these conventions will affect the expression of the tunnel ionization amplitude and rate. Section II B provides a concise description of the DM-SDI model, which is the essential part of this section. Section II C and Sec. II D provide data and computational details about electronic structures and structure parameters of orbitals, respectively.

A. Conventions

In literature dealing with tunnel ionization of nonlinear molecules (for example, Refs. [36,46,47]), there are different conventions for Euler angles, vectors in spherical basis, and phases in orbital wave functions. Therefore, it is important to clarify the conventions used throughout this paper. The coordinates in the laboratory frame (LF) and in the molecular frame (MF) are labeled without prime (x, y, z) and with prime (x', y', z'), respectively.

1. Euler angles

For the Euler angles rotation, we adopt the convention used by Morrison and Parker [48]. An *active* viewpoint is assumed in which a physical system is rotated instead of the reference frame. We chose to rotate the system about the *fixed* axes, i.e., the axes in the LF. The rotations are performed as follows:

(1) Rotate through an angle γ about the z axis,

(2) Rotate through an angle β about the y axis,

(3) Rotate through an angle α about the z axis,

where $0 \leqslant \alpha \leqslant 2\pi$, $0 \leqslant \beta \leqslant \pi$, and $0 \leqslant \gamma \leqslant 2\pi$.

Following the convention in Ref. [48], the spherical harmonics in the MF is transformed to the LF by

$$Y_l^m(\hat{r}') = \sum_{m'=-l}^{l} Y_l^{m'}(\hat{r}) D_{m'm}^l(\alpha, \beta, \gamma), \qquad (1)$$

where $D_{m'm}^l$ is the Wigner D matrix.

We note that the above D matrix $D_{m'm}^l(\alpha, \beta, \gamma)$ is equivalent to the D matrix used in Tolstikhin *et al.* [47] but corresponds to $D_{m'm}^l(-\phi, \theta, -\chi)$ in Zhao *et al.* [46] and $D_{m'm}^l(-\gamma, -\beta, -\alpha)$ in Ref. [36], respectively.

2. Transformation of dipole moments

From quantum chemistry calculations, we obtain the dipole moments in the MF. However, as molecules are randomly oriented in space, their interaction with the laser field defined in the LF varies for different orientations. Therefore, it is important to transform the dipole moments to the LF.

Expressing the dipole moment in the MF, we have

$$\vec{d} = d_-' \hat{\epsilon}'^- + d_0' \hat{\epsilon}'^0 + d_+' \hat{\epsilon}'^+, \qquad (2)$$

where the spherical basis vectors are

$$\hat{\epsilon}'^{\pm} = \mp(\hat{\epsilon}'_x \pm i\hat{\epsilon}'_y)/\sqrt{2},$$

$$\hat{\epsilon}'^0 = \hat{\epsilon}'_z,$$

and the spherical components are related to the MF Cartesian components as

$$d_{\pm}' = (\mp d_x' + id_y')/\sqrt{2},$$

$$d_0' = d_z'.$$

Since the spherical basis vectors transform as $Y_1^m(\hat{r}')$, using Eq. (1), we have

$$\hat{\epsilon}'^\mu = \sum_{\nu=-1}^{1} \hat{\epsilon}^\nu D_{\nu\mu}^1(\alpha, \beta, \gamma).$$

Substituting this expression into Eq. (2), we have

$$\vec{d} = \sum_{\nu=-1}^{1} \left[\sum_{\mu=-1}^{1} d_\mu' D_{\nu\mu}^1(\alpha, \beta, \gamma) \right] \hat{\epsilon}^\nu.$$

For a linearly polarized laser in the z direction, we only need the $\hat{\epsilon}^0$ component of $\vec{d}$, in which

$$d_z(\alpha, \beta, \gamma) = \sum_{\mu=-1}^{1} d_\mu' D_{0\mu}^1(\alpha, \beta, \gamma). \quad (3)$$

Note that α can be set to zero due to the axial symmetry of the laser field.

Sometimes the spherical components of the vector are instead defined as $\tilde{d}_\pm = \mp (d_x \pm i d_y)/\sqrt{2}$ with $\tilde{d}_0 = d_0$. Using $d_\mu = (-1)^\mu \tilde{d}_{-\mu}$, it can be shown that

$$d_z(\alpha, \beta, \gamma) = \sum_{\mu=-1}^{1} \tilde{d}_\mu' D_{0\mu}^{1*}(\alpha, \beta, \gamma).$$

Last, as shown in the work by Yuan *et al.* [49], the phase of transition dipole moment (TDM) could strongly affect the laser-molecule interaction. Since the electronic wave functions are defined up to a sign from quantum chemistry calculations, without time-dependent *ab initio* approaches or experimental data for benchmarking, there is no justification for picking one sign over the other in the modeling. In this work, we choose to normalize the largest component of each TDM to be positive.

3. Expression for tunnel ionization amplitude

In adiabatic tunnel ionization (TI) theories [46,47,50], one expands the asymptotic orbital wave function in the MF as

$$\varphi(\vec{r}') = \sum_{lm'} C_{lm'} F(r) Y_l^{m'}(\hat{r}'), \quad (4)$$

where $F(r \to \infty) \approx r^{Z/\kappa-1} e^{-\kappa r}$, Z is the effective charge after ionization, $\kappa = \sqrt{2I_p}$ with I_p being the ionization potential, and $C_{lm'}$ is the structure parameter. Transforming the spherical harmonics to the LF using Eq. (1), we have

$$\varphi(\vec{r}) = \sum_{lm} \left[\sum_{m'} C_{lm'} D_{mm'}^l(\alpha, \beta, \gamma) \right] F(r) Y_l^m(\hat{r}).$$

For the electric field $F(t) < 0$ and $F(t) > 0$, electron will be emitted along $\theta \sim 0$ and $\theta \sim \pi$, and $Y_l^m(\hat{r})$ takes the asymptotic form [51]

$$Y_l^{\pm m}(\theta \to 0, \phi) \approx Q(l, m) \frac{\sin^{|m|} \theta}{2^{|m|} |m|!} \frac{e^{\pm im\phi}}{\sqrt{2\pi}},$$

$$Y_l^{\pm m}(\theta \to \pi, \phi) \approx (-1)^{l-m} Y_l^{\pm m}(\theta \to 0, \phi),$$
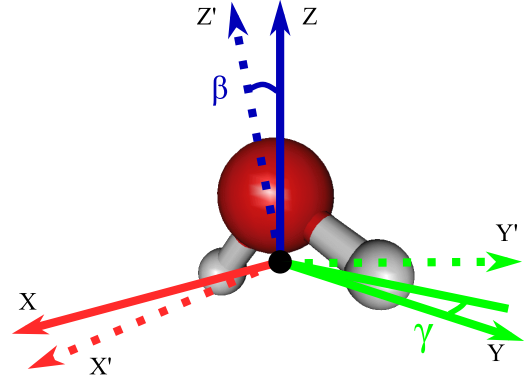

FIG. 1. Definition of the water molecule geometry and the Euler angles used in this work. The water molecule is on the $y'z'$ plane, with the H-H bond along the y' axis. We adopted the z-y-z extrinsic rotation as the convention for Euler angles. Because the laser is linearly polarized along the z axis, the Euler angle α is set to zero.

with

$$Q(l, m) = (-1)^{(m+|m|)/2} \sqrt{\frac{2l+1}{2} \frac{(l+|m|)!}{(l-|m|)!}}.$$

We then identify the B_m parameter in TI theories [46,47,50] as

$$B_m(t) = \sum_{lm'} \text{sgn}[-F(t)]^{l-m} C_{lm'} D_{mm'}^l(\alpha, \beta, \gamma) Q(l, m),$$

where $\text{sgn}[-F(t)] = \pm 1$ for $F(t) < 0$ or $F(t) > 0$. Note that the expression is different from Ref. [36] due to different conventions used.

The TI amplitude can then be expressed as [36,47]

$$\gamma_m(t) = \frac{B_m(t)}{\sqrt{2^{|m|} |m|!}} \frac{1}{\kappa^{Z/\kappa-1/2}} \left[\frac{2\kappa^3}{|F(t)|} \right]^{Z/\kappa-(|m|+1)/2}$$

$$\times \exp\left[-\mu_z(t)\kappa - \frac{\kappa^3}{3|F(t)|} \right]$$

$$\times \exp\left[i\pi \left(\frac{1}{4} + \frac{Z}{\kappa} - \frac{|m|+1}{2} \right) \right], \quad (5)$$

where $\mu_z(t) = d_z(\beta, \gamma) \text{sgn}[F(t)]$ is the effective permanent dipole moment of the orbital [cf. Eq. (3)].

The buildup of coherence and population from multiorbital TI involves the product $\gamma_{im}(t)\gamma_{jm}^*(t)$ for orbitals i and j [36]. Expressing $D_{mm'}^l(\alpha, \beta, \gamma) = e^{-im\alpha} d_{mm'}^l(\beta) e^{-im'\gamma}$, we observe that

$$\gamma_{im}(t)\gamma_{jm}^*(t) \propto B_{im}(t) B_{jm}^*(t)$$

$$= \sum_{l_i m_i'} \text{sgn}[-F(t)]^{l_i} C_{l_i m_i'}^{(i)} d_{mm_i'}^{l_i}(\beta) e^{-im_i'\gamma} Q(l_i, m)$$

$$\times \sum_{l_j m_j'} \text{sgn}[-F(t)]^{l_j} C_{l_j m_j'}^{(j)*} d_{mm_j'}^{l_j}(\beta) e^{im_j'\gamma} Q(l_j, m),$$

such that $\gamma_{im}(t)\gamma_{jm}^*(t)$ does not depend on the Euler angle α, as in the case of LF dipole moments (3). Therefore, for linearly polarized laser field interacting with general molecules, we only need to consider the Euler angles β and γ (see Fig. 1 for example).

Another important observation is that $\gamma_{im}(t)\gamma_{jm}^*(t)$ depends on the relative phase between orbital i and j. Since orbital wave functions are obtained by solving some eigenvalues problems, the wave functions are defined up to an overall phase factor. As a result, $\gamma_{im}(t)\gamma_{jm}^*(t)$ is defined up to an arbitrary phase factor $e^{i\phi_{ij}}$, in which different choices can again affect the laser-molecule interaction. A phase convention is needed to remove this ambiguity. In this work, we define the phase factor by normalizing the structure parameter with the largest magnitude to be real and positive. If that parameter is degenerate over m, then the $-|m|$ component is set to be real and positive.

B. The DM-SDI model

Since comprehensive descriptions of the DM-SDI model can be found in Refs. [27,36], here we only summarize the key aspects of the model. The main assumptions of the model are (1) nuclei of the molecule are fixed in the presence of a few-cycle IR pulse and (2) the ionized electrons are neglected, such that the residual ion and dication become open systems. To describe the evolution of these open systems, we solve the equations of motion for density matrices $\rho^{(q)}$ of charge q,

$$\frac{d}{dt}\rho^{(q)}(t) = -\frac{i}{\hbar}[H^{(q)}(t), \rho^{(q)}(t)] + \Gamma^{(q)}(t), \qquad (6)$$

where $H^{(q)} = H_0^{(q)} - \vec{d}^{(q)} \cdot \vec{E}$ is the Hamiltonian with the field-free term and the laser coupling term and $\Gamma^{(q)}$ is the ionization matrix.

The ionization matrix for the neutral describes depopulation to the ion,

$$\Gamma^{(0)}(t) = -\sum_i \rho^{(0)}(t)W_i^{(0)}(t), \qquad (7)$$

where $W_i^{(0)} = \sum_m |\gamma_{im}^{(0)}(t)|^2$ [cf. Eq. (5)] is the weak-field asymptotic theory (WFAT) TI rate [47] to form the ith ionic state.

For the ion, the ionization matrix $\Gamma^{(1)}$ is

$$\Gamma_{ij}^{(1)}(t) = \rho^{(0)}(t)\sum_m \gamma_{im}^{(0)}(t)\gamma_{jm}^{(0)*}(t)$$
$$- \rho_{ij}^{(1)}(t)\sqrt{\sum_k W_{k\leftarrow i}^{(1)}(t)}\sqrt{\sum_k W_{k\leftarrow j}^{(1)}(t)}, \qquad (8)$$

where the first term describes the buildup of population and coherence from TI of the neutral and the second term describes the depopulation and dephasing from TI to the dication. The TI rate $W_{k\leftarrow i}^{(1)}$ is given by $\sum_m |\gamma_{k\leftarrow i,m}^{(1)}|^2$, with $\gamma_{k\leftarrow i,m}^{(1)}$ being the ionization amplitude from the ith state of the ion to the kth state of the dication with magnetic quantum number m.

In the first term of Eq. (8), the buildup of the tunnel ionization coherence (TIC) is modeled as the inner product of the ionization amplitude $\gamma_{im}^{(0)}$ and $\gamma_{jm}^{(0)}$ [36]. The assumptions behind the model are that ionized electrons from different orbitals (1) are formed at approximately the same time, (2) evolve identically under the strong-field approximation, such that the ionic coherence at a later time is the same as the ionic coherence right after tunneling, and (3) share the same

transverse kinetic energy distribution but have different angular distributions, which is represented by the magnetic quantum number m. Therefore, tracing $\gamma_{im}^{(0)}\gamma_{jm}^{(0)*}$ over m is approximately tracing the amplitudes over the momentum space, resulting in the residual ionic coherence. Meanwhile, in the second term of Eq. (8), the dephasing between state i and j follows the total TI rate from both states, assuming $\rho_{ij}^{(1)} \propto \sqrt{\rho_{ii}^{(1)}\rho_{jj}^{(1)}}$. For $i = j$, the first and second terms of Eq. (8) describe the population changes of the ith state due to TI from the neutral and to the dication, respectively.

Finally, the ionization matrix for the dication describes the buildup of population and coherence from TI of the ion,

$$\Gamma_{kl}^{(2)}(t) = \sum_i \rho_{ii}^{(1)}(t)\sum_m \gamma_{k\leftarrow i,m}^{(1)}(t)\gamma_{l\leftarrow i,m}^{(1)*}(t), \qquad (9)$$

where the TIC is modeled similarly as in Eq. (8). Note that $\Gamma^{(2)}$ is not explicitly dependent on the ionic coherence because tunnel ionization is assumed to be a single-active-electron process.

Setting the initial conditions as $\rho^{(0)}(t_0) = 1$ and $\rho^{(1)}(t_0) = \rho^{(2)}(t_0) = 0$, Eq. (6) for each charge state at each molecular orientation (β, γ) are solved using the classic Runge-Kutta method. At the end of the IR pulse, dication yields are obtained from the diagonal elements of $\rho^{(2)}(\beta, \gamma)$. The orientation-averaged yield P_k is obtained by

$$P_k = \frac{1}{4\pi}\int_0^{2\pi}\int_0^{\pi}\rho_{kk}^{(2)}(\beta, \gamma)\sin\beta\, d\beta d\gamma, $$

assuming an isotropic distribution of the orientation.

In principle, with the knowledge of orientation-dependent dication yield, observables such as kinetic energy release and branching ratio of different fragmentation channels can be obtained. However, from the investigations on single-photon double ionization [44,45] and strong-field double ionization [16,17] of water, it is clear that the dissociation of dications formed from SDI cannot be described a field-free process. Therefore, we reserve the mapping of the calculated dication yields to experimental observables for future studies. Here we will focus on the formation mechanisms of different water dication states from SDI.

C. Electronic structures of water

Since the potential energy surfaces of several H_2O^{2+} states have been extensively investigated by Gervais *et al.* [52], we adopt their calculated vertical ionization potentials here. Examples of potential energy surfaces can be found in Fig. 2 of Ref. [44]. Table I summarizes the electronic structures of the H_2O^{2+} states with two valence holes in the $1b_2$, $3a_1$, and $1b_1$ orbitals. For discussions later, we also include the three-body branching ratios 3BR from field-free trajectory calculations in Howard *et al.* [18] and the parents of the dication, which are determined by their electronic configuration.

To obtain the permanent and transition dipole moments of H_2O, H_2O^+, and H_2O^{2+}, we carried out electronic structure calculations at the equilibrium geometry of H_2O with C_1 symmetry in `OpenMolcas` [53]. The C_1 symmetry instead of C_{2v} symmetry was used in the calculations because it ensures that the electronic wave functions with different symmetries are optimized at an equal footing, providing more accurate
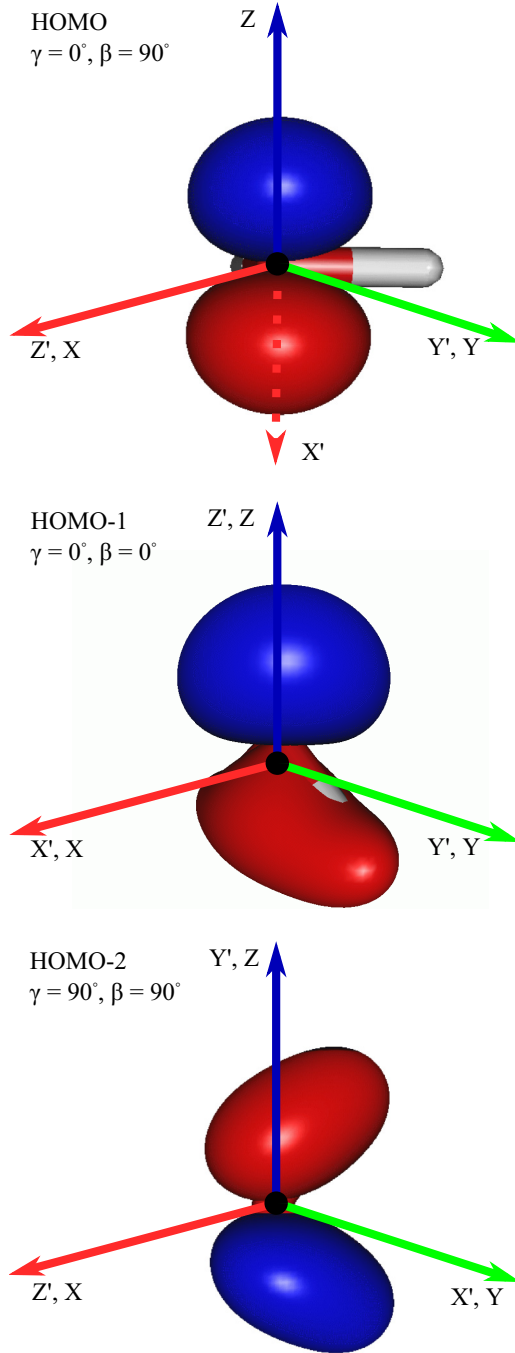
FIG. 2. Visualization of the highest occupied molecular orbital (HOMO) ($1b_1$, top), HOMO-1 ($3a_1$, middle), and HOMO-2 ($1b_2$, bottom) of H_2O. The molecule is rotated by Euler angles (β, γ) such that the orbitals are parallel to the laser polarization along the z axis. One shall expect that ionization rate of the HOMO, HOMO-1, and HOMO-2 would be maximized at ($\beta = 90°, \gamma = 0°$), ($\beta = 0/180°$), and ($\beta = 90°, \gamma = 90°$), respectively. See Fig. 1 for the definition of Euler angles.

transition dipole moments. The molecule is fixed on the $y'z'$ plane with two OH bonds at 0.958 Å and the HOH bond angle at 104.5° (see Fig. 1). The O $1s$ electrons are kept frozen and the rest of the eight, seven, or six electrons in H_2O, H_2O^+, or H_2O^{2+} are in the active space, which consists of the $2a_1$, $1b_2$,

TABLE I. Electronic structures of the H_2O^{2+} states with two valence holes in the $1b_2$, $3a_1$, and $1b_1$ orbitals. The vertical ionization potential I_p and the three-body branching ratios 3BR are extracted from Howard *et al.* [18]. Possible parents of the dication states are also listed.

#	State	Config.	I_p (eV)	3BR(%)	Parent(s)
0	$^3B_1$	$3a_1^{-1}1b_1^{-1}$	40.3	7.0	X^2B_1, A^2A_1
1	$^1A_1$	$1b_1^{-2}$	41.4	0.6	X^2B_1
2	$^1B_1$	$3a_1^{-1}1b_1^{-1}$	42.8	12.3	X^2B_1, A^2A_1
3	$^3A_2$	$1b_2^{-1}1b_1^{-1}$	44.3	100.0	A^2B_1, B^2B_2
4	2^1A_1	$3a_1^{-2}$	46.0	73.7	A^2A_1
5	$^1A_2$	$1b_2^{-1}1b_1^{-1}$	46.0	100.0	X^2B_1, B^2B_2
6	$^3B_2$	$1b_2^{-1}3a_1^{-1}$	46.3	100.0	A^2A_1, B^2B_2
7	$^1B_2$	$1b_2^{-1}3a_1^{-1}$	48.4	100.0	A^2A_1, B^2B_2
8	3^1A_1	$1b_2^{-2}$	53.6	100.0	B^2B_2

$3a_1$, and $1b_1$ orbitals and seven lowest unoccupied orbitals. We used the large Atomic Natural Orbital basis for both the O and H atoms and calculated the electronic wave functions with the state-averaged complete active space self-consistent field method. For H_2O, only one electronic state is considered. For H_2O^+ and the triplet H_2O^{2+}, three electronic states are included, while for the singlet H_2O^{2+}, 6 electronic states are included. We then performed the second-order perturbation (CASPT2) calculation to further improve the accuracy of the electronic energies for states identification. The calculated permanent and transition dipole moments for H_2O, H_2O^+, and H_2O^{2+} are tabulated in Table II. For convenience, hereafter, we refer the $\tilde{X}$ state to the X^1A_1 state of H_2O. The X, A, and B states refer to the X^2B_1, A^2A_1, and B^2B_2 states of H_2O^+. States 0–8 refer to the 9 H_2O^{2+} states. The above calculations produce accurate electronic energies, which are on average less than 5% in relative errors for H_2O^+ as compared with experiments [54] and for H_2O^{2+} as compared with Gervais *et al.* [52].

D. Structure parameters of water

Before getting into the calculations of structure parameters of the three highest occupied molecular orbitals (HOMO)—$1b_1$ (HOMO), $3a_1$ (HOMO-1), and $1b_2$ (HOMO-2)—it is instructive to inspect the shape of the orbitals. Figure 2 shows the three HOMOs rotated by some Euler angles (β, γ), which is defined in Fig. 1. We can see that when ($\gamma = 0°, \beta = 90°$), $\beta = 0°$ or $180°$, and ($\gamma = 90°, \beta = 90°$), the nodal plane of HOMO, HOMO-1, and HOMO-2 is perpendicular to the laser-field direction (along the z axis), respectively. We can then deduce that their ionization rates should be maximized around these angles if linear Stark shift due to their permanent dipole moment is negligible.

To determine the structure parameters in Eq. (4), asymptotic orbital wave functions are required. In this work, we calculated orbital wave functions using the density functional theory software `Octopus` [55], which represents the Kohn-Sham orbitals on real-space grids. Using the corrected exchange density with the local density approximation [56], the asymptotic behavior for the Coulomb potential is properly imposed for Kohn-Sham orbitals. It has been demonstrated

TABLE II. Dipole moments $\vec{d}_{ij}$ (in atomic unit) with magnitude larger than 10^{-2} for all charge states ($q = 0, 1, 2$) of H_2O, calculated in this work. $\tilde{X}$ is the ground electronic state of the neutral, X, A, and B are the ionic states considered, and state 0–8 are the dication states defined in Table I. For $i \neq j$, the largest component of $\vec{d}_{ij}$ is chosen to be positive.

q	i	j	d_x	d_y	d_z
0	$\tilde{X}$	$\tilde{X}$	0.000	0.000	−0.737
1	X	X	0.000	0.000	−0.832
1	X	A	0.148	0.000	0.000
1	A	A	0.000	0.000	−0.633
1	A	B	0.000	0.071	0.000
1	B	B	0.000	0.000	−1.030
2	0	0	0.000	0.000	−1.701
2	0	3	0.000	0.020	0.000
2	1	1	0.000	0.000	−2.182
2	1	2	0.121	0.000	0.000
2	1	5	0.000	0.000	0.085
2	1	7	0.000	0.022	0.000
2	2	2	0.000	0.000	−1.959
2	2	4	0.000	0.058	0.000
2	2	5	0.150	0.000	0.000
2	2	8	0.012	0.000	0.000
2	3	3	0.000	0.000	−2.684
2	3	6	0.130	0.000	0.000
2	4	4	0.000	0.000	−2.615
2	4	7	0.143	0.000	0.000
2	5	5	0.000	0.000	−1.683
2	5	7	0.000	0.082	0.000
2	5	8	0.000	0.000	0.067
2	6	6	0.000	0.000	−2.129
2	7	7	0.000	0.000	−2.122
2	7	8	0.000	0.078	0.000
2	8	8	0.000	0.000	−3.077

that this approach yields orbital energies close to experimental ionization potentials for several atoms [56]. Since this approach can also calculate orbitals of excited states and open-shell targets, it could be used to obtain the structure parameters of molecular orbitals of different states required for the DM-SDI model.

A comprehensive discussion on this approach for the determination of structure parameters is out of the scope of this work. Here we only describe the results we obtained for three HOMOs of H_2O and H_2O^+.

Table III shows the calculated binding energies and structure parameters of the above orbitals of the $\tilde{X}$ state of H_2O. The calculated binding energies differ from the experimental ionization potentials [54] only by less than 4%. Note that we applied the phase convention mentioned in Sec. II A 3, where the structure parameter with the largest magnitude and the smallest m is real and positive.

Table IV shows the calculated binding energies and structure parameters of three HOMOs of the X state of H_2O^+, assuming a spin-down electron is ionized from HOMO. Since the X state is a doublet, the binding energies of spin-up or spin-down electrons in HOMO-1 and HOMO-2 are different. In Table IV, we consider only the case when a spin-down

TABLE III. Structure parameters C_{lm} and binding energies E_b of the $1b_1$, $3a_1$, and $1b_2$ orbitals of the neutral H_2O calculated in this work. Experimental vertical ionization potentials I_p to the corresponding H_2O^+ states [54] are also listed.

Orb.	E_b (eV)	I_p (eV)	C_{lm}			
$1b_1$	12.2	12.6	$C_{1\mp1}$ ±0.79	$C_{2\mp1}$ ∓0.05	$C_{3\mp3}$ ∓0.03	
$3a_1$	14.2	14.8	C_{00} −0.20	C_{10} 1.64	$C_{2\mp2}$ 0.12	C_{20} −0.08
			$C_{3\mp2}$ −0.07	C_{30} −0.03	$C_{4\mp2}$ 0.01	C_{40} 0.01
$1b_2$	18.2	18.7	$C_{1\mp1}$ 2.06	$C_{2\mp1}$ −0.50	$C_{3\mp3}$ −0.13	
			$C_{3\mp1}$ 0.03	$C_{4\mp3}$ 0.04	$C_{4\mp1}$ 0.03	

electron is ionized from HOMO-1 or HOMO-2, forming the $^3B_1$ or $^3A_2$ states. The $^1A_1$ state is formed by ionizing the spin-up electron from HOMO. As in the case of the $\tilde{X}$ state, the calculated binding energies differ only by less than 4% compared to the difference between the I_p of $^3B_1$, $^1A_1$, and $^3A_2$ states to the X state. The structure parameters for HOMO, HOMO-1, and HOMO-2 of the X states are about 120%, 77%, and 56% larger than those of the $\tilde{X}$ state. Since the TI rate scales with $|C_{lm}|^2$, it is important to account for such changes in the modeling.

For the spin-up electrons in HOMO-1 and HOMO-2, the calculated binding energies agree well with the energy difference between states 2 and 5 to the X state: There are only 7.5% and 5.1% differences. The structure parameters only differ by less than 2% compared to the spin-down cases. Therefore, it is reasonable to use the structure parameters of the spin-down electrons for the spin-up one.

By placing the hole in HOMO to HOMO-1 or HOMO-2 in the calculations, results of the three HOMOs of the A and B states were obtained. The ΔSCF excitation energies from the X state to the A and B states are 2.02 and 6.08 eV, respectively, in excellent agreement with the experimental values of 2.2

TABLE IV. Structure parameters C_{lm} and binding energies E_b of the $1b_1$, $3a_1$, and $1b_2$ orbitals of the X^2B_1 state calculated in this work. The effective I_p of the $1b_1$, $3a_1$, and $1b_1$ orbitals are obtained by subtracting the I_p to the 1^1A_1, $^3B_1$, and $^3A_2$ states by the I_p to the X^2B_1 state, respectively.

Orb.	E_b (eV)	I_p (eV)	C_{lm}				
$1b_1$	27.9	28.8	$C_{1\mp1}$ ±1.73	$C_{2\mp1}$ ∓0.04	$C_{3\mp3}$ ∓0.06	$C_{3\mp1}$ ±0.01	$C_{4\mp3}$ ±0.02
$3a_1$	26.9	27.7	C_{00} −0.16	C_{10} 2.90	$C_{2\mp2}$ 0.24	C_{20} −0.08	$C_{3\mp2}$ −0.14
			C_{30} −0.08	$C_{4\mp4}$ −0.01	$C_{4\mp2}$ 0.04	C_{40} 0.04	
$1b_2$	30.9	31.7	$C_{1\mp1}$ 3.22	$C_{2\mp1}$ −0.77	$C_{3\mp3}$ −0.22	$C_{3\mp1}$ 0.05	$C_{4\mp3}$ 0.09
			$C_{4\mp1}$ 0.06	$C_{5\mp5}$ 0.01	$C_{5\mp3}$ −0.02	$C_{5\mp1}$ −0.02	

TABLE V. Orientation-averaged dication yields of H_2O^{2+} states in Table I calculated using different models. PDM: Permanent dipole moment. TDM: Transition dipole moment. TIC: Tunnel ionization coherence. The numbers followed PDM/TDM/TIC represent levels of the theory. 0 means it is neglected. 1 means it is considered for the neutral and the ion. 2 means it is considered for all charge states. The highest level of theory, `PDM2-TDM2-TIC2`, is marked by ∗.

Models/states	$^3B_1$	$^1A_1$	$^1B_1$	$^3A_2$	$2\,^1A_1$	$^1A_2$	$^3B_2$	$^1B_2$	$3\,^1A_1$	Total
`PDM0-TDM0-TIC0`	2.55^{-1}	7.91^{-2}	3.56^{-2}	3.41^{-2}	8.67^{-3}	8.74^{-3}	2.00^{-2}	3.73^{-3}	2.28^{-4}	0.445
`PDM2-TDM0-TIC0`	2.95^{-1}	1.44^{-1}	6.75^{-2}	6.58^{-2}	9.97^{-2}	7.39^{-3}	2.39^{-2}	4.59^{-3}	4.45^{-4}	0.708
`PDM2-TDM1-TIC0`	4.14^{-1}	9.21^{-2}	8.81^{-2}	6.04^{-2}	1.03^{-1}	6.65^{-3}	2.68^{-2}	5.13^{-3}	4.69^{-4}	0.796
`PDM2-TDM2-TIC0`	4.13^{-1}	8.13^{-2}	9.50^{-2}	5.20^{-2}	9.87^{-2}	1.19^{-2}	3.53^{-2}	7.54^{-3}	6.79^{-4}	0.796
`PDM2-TDM2-TIC1`	4.10^{-1}	8.17^{-2}	9.52^{-2}	5.39^{-2}	9.72^{-2}	1.19^{-2}	3.55^{-2}	7.45^{-3}	6.89^{-4}	0.794
`PDM2-TDM2-TIC2`∗	4.11^{-1}	1.05^{-2}	7.37^{-2}	5.14^{-2}	9.36^{-2}	1.27^{-2}	3.76^{-2}	7.96^{-3}	7.17^{-4}	0.794

and 6.1 eV [54]. We also verified that all binding energies agree within 8% compared to the effective binding energies calculated using I_p in Table I and III. Since the structure parameters of the three HOMOs of the A and B states only differ by less than 15% compared to the X state, it is sufficient to use the structure parameters in Table IV for orbitals of these excited states.

III. RESULTS AND DISCUSSION

To understand the mechanism of SDI of water, we present calculated dication yields at different levels of theory. The levels of theory are controlled by the consideration of permanent dipole moments (PDM), transition dipole moments (TDM), and tunnel ionization coherence (TIC). For convenience, we name the theories by `PDMa-TDMb-TICc`, where `a`, `b`, and `c` can be `0`,`1`, or `2`. In the above, `0` means that quantity is neglected for all charge states, `1` means that quantity is considered for the neutral and the ion, and `2` means that quantity is considered for all charge states. The laser pulse is assumed to be linearly polarized with a Gaussian envelope, a central wavelength of 750 nm, a pulse duration of 6 fs, and a peak intensity of $1\,\mathrm{PW/cm^2}$. The water molecule is assumed to be randomly oriented in space. In the following subsections, we will discuss the influence of PDM, TDM, and TIC on SDI of water.

The orientation-averaged dication yields from different theories are summarized in Table V. We can see that total dication yield increases as we increase the level of theory from `PDM0-TDM0-TIC0` to `PDM2-TDM1-TIC0`. Some averaged dication yields increase significantly as we increase the level of theory as well. The orientation-dependent dication yields calculated using the highest level of theory, `PDM2-TDM2-TIC2`, are showcased in Fig. 3. Since water molecule possesses the C_{2v} symmetry, it is sufficient to consider γ from 0 to 90°. Their angular distributions are very different from the expectation based on orbital structures in Fig. 2, except for the $2\,^1A_1$ state. It would be interesting to investigate the formation mechanisms of the dication states using a bottom-up, anatomy approach. Since the yield of the $^1B_2$ and $3\,^1A_1$ states are negligible, their formation mechanisms will not be discussed.

A. Influence of permanent dipole moment

To study the influence of PDMs in SDI of water, we consider the models `PDM0-TDM0-TIC0` and `PDM2-TDM0-TIC0`. A

comparison of these two models can show how PDMs modify the WFAT TI rates. At such low level of theory, Eq. (6) reduces to a set of rate equations,

$$\frac{d}{dt}\rho^{(q)}(t) = A^{(q)}(t), \tag{10}$$

with $A^{(0)} = \Gamma^{(0)}$ in Eq. (7),

$$A_{ij}^{(1)}(t) = \delta_{ij}\big[\rho^{(0)}(t)W_i^{(0)}(t) - \rho_{ii}^{(1)}(t)W_{k\leftarrow i}^{(1)}(t)\big], \tag{11}$$

and

$$A_{kl}^{(2)}(t) = \delta_{kl}\sum_i \rho_{ii}^{(1)}(t)W_{k\leftarrow i}^{(1)}(t). \tag{12}$$

Consequently, the models `PDM0-TDM0-TIC0` and `PDM2-TDM0-TIC0` describe SDI as an incoherent process.

The dominant effect of PDMs is the linear Stark shift in electronic energy. For the ith state, the electronic energy is

$$E_i(\beta, \gamma, t) = E_{i0} - d_{z,ii}(\beta, \gamma)F_z(t),$$

where E_{i0} is the field-free electronic energy, $d_{z,ii}(\beta, \gamma)$ is the PDM in Table II rotated to the LF by Eq. (3), and F_z is the electric field. The effective ionization potential for each orbital (to reach state f) is then

$$
\begin{aligned}
I_p(\beta, \gamma, t) &= E_f(\beta, \gamma, t) - E_i(\beta, \gamma, t) \\
&= I_{p0} + [d_{z,ii}(\beta, \gamma) - d_{z,ff}(\beta, \gamma)]F_z(t).
\end{aligned}
$$

Assuming the linear Stark shift is small, the effective I_p goes into the exponent in the TI rate as $\exp\left[-2\mu_z(t)\kappa - 2\kappa^3/(3|F_z(t)|)\right]$ [47,57], with effective PDM for the ionized orbital

$$\mu_z(t) = [d_{z,ii}(\beta, \gamma) - d_{z,ff}(\beta, \gamma)]\mathrm{sgn}[F_z(t)]. \tag{13}$$

Note that the PDMs for all charge states in Table II are in the z' direction. Then according to Eq. (3), we have

$$d_{z,ii}(\beta, \gamma) = d_{z,ii}'\cos\beta,$$

such that the linear Stark shift is independent of γ for water.

From Table V, we see that the PDMs play a critical role in enhancing the dication formation. The total dication yield calculated by the `PDM2-TDM0-TIC0` model is about 60% more compared to the results calculated by the `PDM0-TDM0-TIC0` model. Looking into individual dication states, we see that the $^1A_1$, $^1B_1$, and $^3A_2$ states yield is enhanced by 82%, 89%, and 94% when the PDM is considered. Remarkably, the yield of the $2\,^1A_1$ state is enhanced by an order of magnitude. It
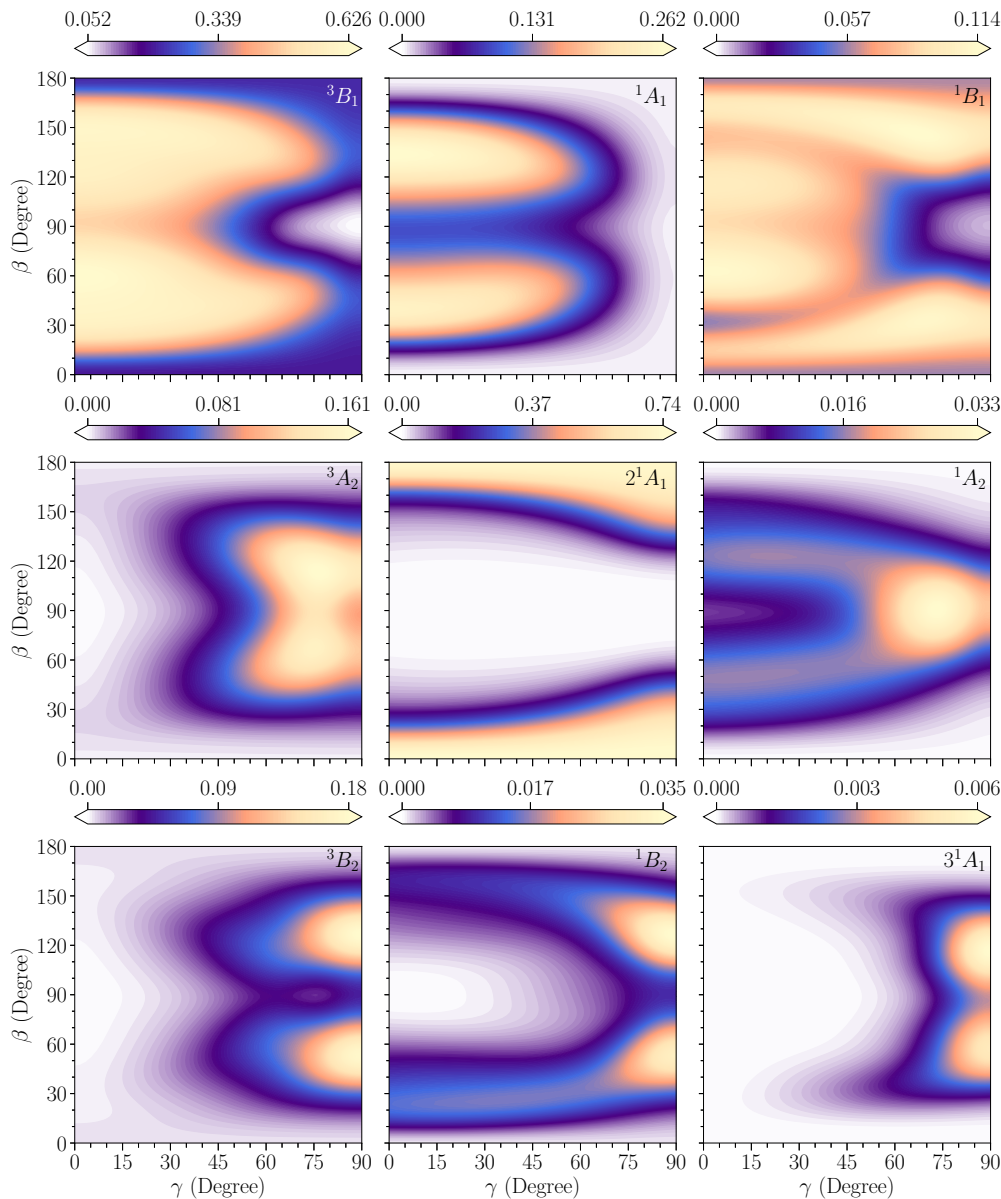
FIG. 3. Orientation-dependent dication yields for states 0–8 in Table I, calculated using the `PDM2-TDM2-TIC2` model. The angular distribution of the 2^1A_1 state follows the expectation from Fig 2: The yield is maximized when $\beta = 0$ and $180°$, insensitive of the value of γ. However, angular distribution of other dication states depart significantly from the expectation of Fig. 2, suggesting that there are rich dynamics in SDI of water.

is therefore of interest to examine the orientation-dependent yield of these states to explain such enhancement.

Figure 4 shows the orientation-dependent yield of the $^1A_1$, 2^1A_1, 3^1A_1, $^1B_1$, $^3A_2$, and $^3B_2$ states. Note that the triplet or singlet counterpart of these states, if any, has the same angular distribution here. The orientation-dependent yields from the `PDM2-TDM0-TIC0` model are higher than those from the `PDM0-TDM0-TIC0` model for the entire range of (β, γ). We can also see that the orientation dependence of some states change when PDMs are included.

To understand these distributions, we first inspect the yields of the $^1A_1(1b_1^{-2})$, $2^1A_1(3a_1^{-2})$, and $3^1A_1(1b_2^{-2})$ states from the `PDM0-TDM0-TIC0` model. Their electronic configurations have two holes in the same orbital, such that their angular

distributions reflect the orientation dependence of the WFAT TI rates with zero PDMs. We can see that the TI rate of the $1b_1$, $3a_1$, and $1b_2$ orbitals is indeed peak in the region of $(\beta = 90°, \gamma = 0°)$, $\beta = 0/180°$, and $(\beta = 90°, \gamma = 90°)$, respectively (cf. Fig. 2). In particular, since the $3a_1$ orbital is aligned with the z' axis, the TI rate is rather uniform along γ. Based on such observations, as the $^1B_1$, $^3A_2$, and $^3B_2$ states has configuration $3a_1^{-1}1b_1^{-1}$, $1b_2^{-1}1b_1^{-1}$, and $1b_2^{-1}3a_1^{-1}$, their angular distribution can be simply understood as the product of the angular distribution of the respective orbitals.

As we use the `PDM2-TDM0-TIC0` model, the distributions of the $^1A_1$ and 3^1A_1 show significant changes. Since the linear Stark shift, which is zero at $\beta = 90°$, lowers the effective ionization potential at some times, their maximum yields are
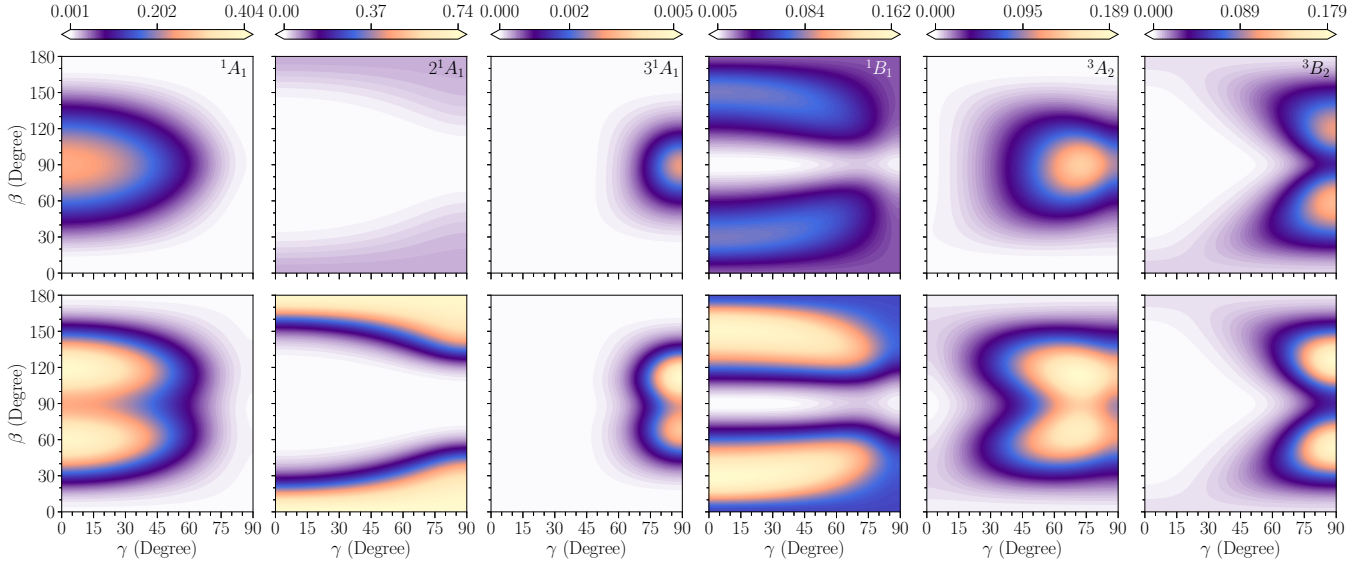
FIG. 4. Top row: Orientation-dependent dication yields for the $^1A_1$, 2^1A_1, 3^1A_1, $^1B_1$, $^3A_2$, and $^3B_2$ states, calculated using the `PDM0-TDM0-TIC0` model. Bottom row: Same yields, but calculated using the `PDM2-TDM0-TIC0` model. The triplet or singlet counterpart (if any) of the above states share the same angular distribution for both models. Results in the top row follow the expectation of Fig. 2. The linear Stark shift significantly enhances the overall dication yield and alters the angular distribution in the results of the bottom row. The angular distribution of the $^3A_2$ and the 2^1A_1 states now agree well with Fig. 3, implying that their formation mechanisms are through linear Stark shift enhanced tunnel ionization.

now increased by about a factor of 2 and peak at around $\beta = 60°$ and 120°. For the 2^1A_1 state, since the yield peaks at $\beta = 0/180°$, where the linear Stark shift is the largest, the maximum yield is enhanced by a factor of 15, while the angular distribution remains unchanged. The change of angular distribution and the enhanced formation of the other states are just the product of the above effects.

To summarize, the inclusion of PDMs and the consideration of linear Stark shift are crucial in modeling SDI of water. Linear Stark shift strongly enhances the dication yields and changes the angular distribution by lowering the ionization potential at different β and time. The enhancement on ionizing the $3a_1$ orbital is much stronger than on ionizing the $1b_1$ and $1b_2$ orbitals. This is because the $3a_1$ orbital is aligned with the z' axis, so that linear Stark shift has the strongest effect on its TI rate. Using the `PDM2-TDM0-TIC0` model, the angular distribution of the $^3A_2$ and the 2^1A_1 states in Fig. 4 now agrees with Fig. 3, implying that their formation mechanism is through linear Stark shift enhanced tunnel ionization.

B. Influence of transition dipole moment

To increase the level of theory, in this subsection, we consider the TDM between cation states and between dication states. The models we will be using in this subsection are `PDM2-TDM1-TIC0` and `PDM2-TDM2-TIC0`. We will first describe the theoretical models and then compare results from `PDM2-TDM1-TIC0` with those from `PDM2-TDM0-TIC0` to examine the influence of laser coupling between cation states. Next, we compare the `PDM2-TDM2-TIC0` results with those from `PDM2-TDM1-TIC0` to investigate the effect of laser couplings between dication states. A summary will be given at the end of this subsection.

The equation of motion for `PDM2-TDM1-TIC0` and `PDM2-TDM2-TIC0` is

$$\frac{d}{dt}\rho^{(q)}(t) = -\frac{i}{\hbar}[H^{(q)}(t), \rho^{(q)}(t)] + B^{(q)}(t). \quad (14)$$

Since tunnel ionization coherence is not included here, the ionization matrices are $B^{(0)} = \Gamma^{(0)}$ in Eq. (7),

$$B_{ij}^{(1)}(t) = \rho^{(0)}(t)\delta_{ij}\sum_k W_{k\leftarrow i}^{(1)}(t)$$
$$- \rho_{ij}^{(1)}(t)\sqrt{\sum_k W_{k\leftarrow i}^{(1)}(t)}\sqrt{\sum_k W_{k\leftarrow j}^{(1)}(t)}, \quad (15)$$

and

$$B_{kl}^{(2)}(t) = \delta_{kl}\sum_i \rho_{ii}^{(1)}(t)W_{k\leftarrow i}^{(1)}(t). \quad (16)$$

Note that while the first term of $B_{ij}^{(1)}$ is diagonal, the off-diagonal elements in the second term are kept in order to describe the dephasing due to depletion of population.

We first compare the orientation-averaged dication yields obtained from `PDM2-TDM1-TIC0` and `PDM2-TDM0-TIC0`. From Table V, we see that the total dication yield is increased by about 12% when TDMs between the cation states are considered. When the TDMs are included, yield of the $^3B_1$ and $^1B_1$ states increases by about 40% and 29%, respectively, while yield of the $^1A_1$ state decreased by about 36%. Since the B_1 states have a hole in both the $3a_1$ and $1b_1$ orbitals, while the $^1A_1$ state has two holes in the $1b_1$ orbital, the results suggest that the transient population of the $X(1b_1^{-1})$ and $A(3a_1^{-1})$ state is suppressed and enhanced, respectively, when the TDMs are included. Hence, the laser coupling between the X and A state plays an important role in water SDI, as was suggested
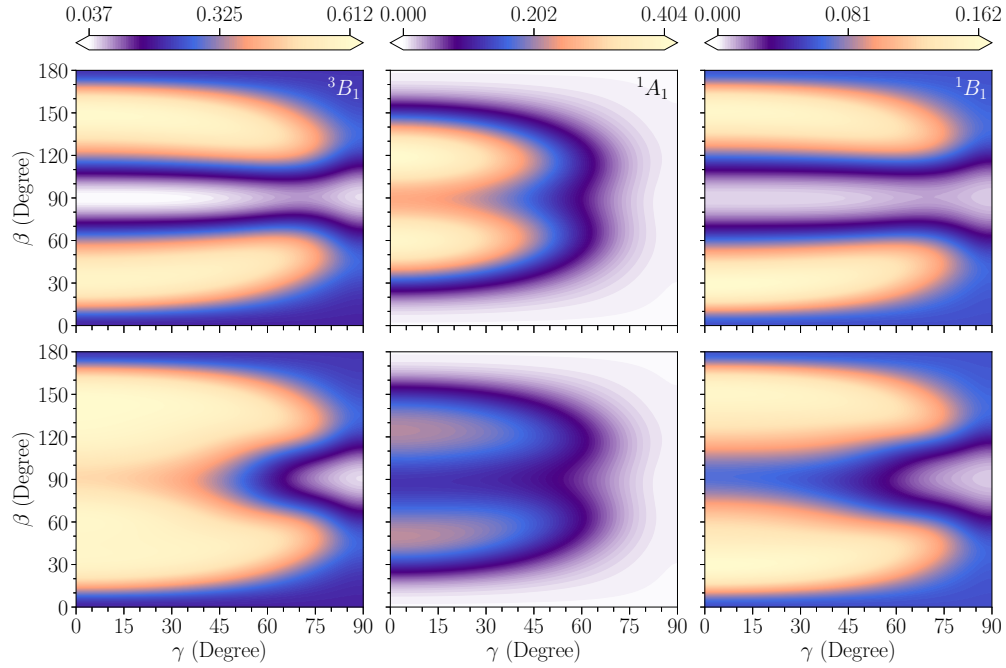
FIG. 5. Top row: Orientation-dependent dication yields for the $^3B_1$, $^1A_1$, and $^1B_1$ states, calculated using the `PDM2-TDM0-TIC0` model. Bottom row: Same yields but calculated using the `PDM2-TDM1-TIC0` model. All other states have very similar distributions and are not shown here. The X-A laser coupling transfers population from the X state to the A state of H_2O^+, enhancing and suppressing formation of the B_1 states and the $^1A_1$ state, respectively. The angular distribution of the $^3B_1$ state now agrees with Fig. 3, implying that the $^3B_1$ state forms via linear Stark shift enhanced tunnel ionization and the X-A laser coupling.

in Ref. [17]. In contrast, yield of the 3^1A_1 state, which has two holes in the $1b_2$ orbital, increases only by about 5% for `PDM2-TDM1-TIC0`. In addition, we see 8–10% decreases on the yield of the $A_2(1b_1^{-1}1b_2^{-1})$ states for `PDM2-TDM1-TIC0`, suggesting that the effect from the suppression of the X state is greater than the enhancement of the $B(1b_2^{-1})$ state. These imply that the A-B coupling only plays a minor role in water SDI. From the above observations, we can deduce that [29] the water SDI process could be used to probe the X-A vibronic coherence, while the influence of A-B vibronic coherence could be too weak to observe.

It is of interest to examine how the X-A laser coupling alters the orientation-dependent dication yields. Figure 5 shows the comparison of orientation-dependent dication yields for the $^3B_1$, $^1A_1$, and $^1B_1$ states, calculated using `PDM2-TDM0-TIC0` and `PDM2-TDM1-TIC0`. The angular yield of other dication states are about the same between these two models and are not shown. We see that the maximum yield of the $^1A_1$ state is decreased by a factor of 2 for `PDM2-TDM1-TIC0`, and the decrease of yield is mainly in the region between $\beta = 30$–$150°$ and $\gamma < 45°$. In contrast, the maximum yield of the B_1 states are about the same for both models, but their formation are enhanced in the same region for `PDM2-TDM1-TIC0`. The population changes for the $^1A_1$ and B_1 states can be understood as follows. Since the X-A TDM is in the x' direction, the laser coupling is the strongest around $\beta = 90°$ and $\gamma = 0°$. The population of the X state in the region of $\beta = 30$–$150°$ and $\gamma < 45°$ is therefore transferred to the A state, which is subsequently tunnel ionized to form the B_1 states. To this end, one can see that the angular distribution

of the $^3B_1$ state in Fig. 5 now agrees with Fig. 3, such that the $^3B_1$ state forms via linear Stark shift enhanced tunnel ionization and the X-A laser coupling.

Next, we compare orientation-averaged dication yields in Table V between the `PDM2-TDM2-TIC0` model and the `PDM2-TDM1-TIC0` model. We first notice that introducing TDMs of the dication does not change the total dication yield, because such laser couplings only transfer population among the dication. While the yield of the $^1B_2$ and 3^1A_1 states increase noticeably, their contributions to the overall yield remain negligible. We observed that the yield of the $^1A_2$ and the $^3B_2$ states increases by about 71% and 30%, respectively. Yield of the other states change by about ± 10%.

To further investigate the postionization dynamics of the singlet dication, we again investigate the orientation-dependent yields. In Table II, we see that the $^1A_1$, $^1B_1$, and $^1A_2$ states are interconnected. The dominant TDMs are the $^1A_1$-$^1B_1$ ($\vec{d}_{12} = 0.121\hat{x}$) and the $^1B_1$-$^1A_2$ ($\vec{d}_{25} = 0.15\hat{x}$) transitions, while the TDM of the $^1A_1$-$^1A_2$ ($\vec{d}_{15} = 0.085\hat{z}$) transition is weaker. Since the $^1A_1$ state is not populated around $\beta = 0/180°$, the $^1A_1$-$^1A_2$ coupling only plays a minor role in the dynamics. In Fig. 6, we see that population of the $^1A_1$ state decreases moderately for $\gamma < 45°$ and $30° < \beta < 150°$ when comparing `PDM2-TDM2-TIC0` to `PDM2-TDM1-TIC0`. This happens in such region again because $^1A_1$-$^1B_1$ and $^1B_1$-$^1A_2$ couplings are the strongest around $\beta = 90°$ and $\gamma = 0°$. The $^1A_1$ population is transferred to the $^1B_1$ state, as can be seen from the enhancement around $\gamma = 0°$ and $\beta = 90°$. Similarly, the yield of the $^1A_2$ state is also enhanced due to the $^1B_1$-$^1A_2$ coupling. Interestingly, the
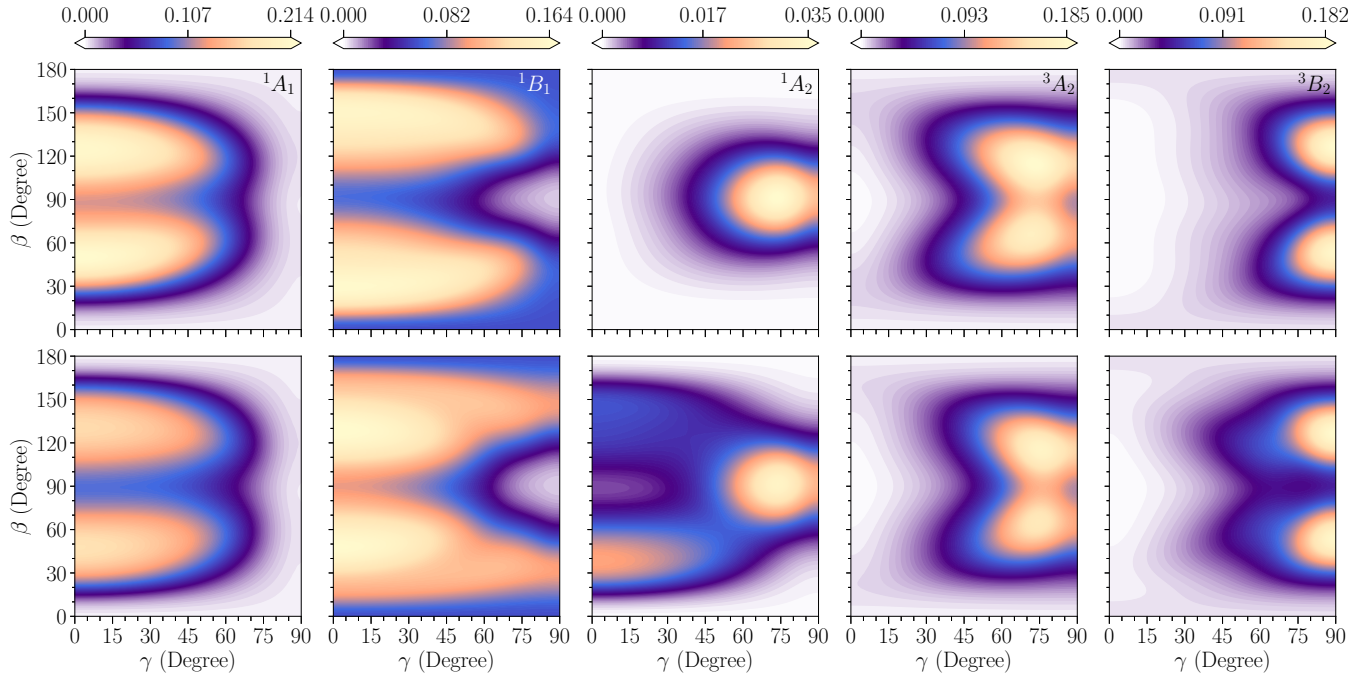
FIG. 6. Top row: Orientation-dependent dication yields for the $^1A_1$, $^1B_1$, $^1A_2$, $^3A_2$, and $^3B_2$ states, calculated using the PDM2-TDM1-TIC0 model. Bottom row: Same yields but calculated using the PDM2-TDM2-TIC0 model. Laser couplings between the dication states further alter the angular distributions of states. One can observe that population of the $^3A_2$ state around ($\beta = 90°$, $\gamma = 45°$) is transferred to the $^3B_2$ state, such that angular distribution of the $^3B_2$ state now agrees with Fig. 3. But there are still disagreements in the distributions of the $^1A_1$, $^1B_1$, and $^1A_2$ states.

yield of the $^1A_2$ state is asymmetric about $\beta = 90°$. In addition to the above dynamics, we observe that the $^1B_1$ population is enhanced around $\gamma = 90°$. This is due to the weak coupling between the $^1B_1$ and 2^1A_1 state ($\vec{d}_{24} = 0.058\hat{y}$), which is the strongest around $\beta = 90°$ and $\gamma = 90°$. While there are significant changes in the $^1A_1$, $^1B_1$, and $^1A_2$ angular distributions with the inclusion of TDMs, they still disagree with Fig. 3.

On the other hand, for the $^3B_2$ state, it is coupled only to the $^3A_2$ state ($\vec{d}_{36} = 0.13\hat{x}$). Therefore, in Fig. 6, population of the $^3A_2$ state around ($\beta = 90°$, $\gamma < 45°$) is transferred to the $^3B_2$ state, resulting in an elongated distribution along γ for the $^3B_2$ state, which now agrees well with Fig. 3.

To summarize, in this subsection, we investigate the influence of laser couplings between cation states and between dication states. We found that, during SDI, the X-A coupling leads to enhanced formation of the A state, while the A-B coupling leads to slightly enhanced formation of the B states. Therefore, we conclude that SDI observables for water should be sensitive to the X-A vibronic coherence but depend only very weakly on the A-B vibronic coherence. We also discovered rich dynamics between the $^1A_1$, $^1B_1$, and $^1A_2$ states, leading to significantly different angular distributions when the laser couplings are switched on.

C. Influence of tunnel ionization coherence

In this subsection, we further increase the level of theory by introducing TIC. Doing so could change the effect of laser couplings, resulting in different angular distributions. We first

include the TIC for the ion using the PDM2-TDM2-TIC1 model and then for the dication using the PDM2-TDM2-TIC2 model.

For the PDM2-TDM2-TIC1 model, we solve Eq. (6) with the ionization matrices in Eqs. (7) and (8) for the neutral and the ion and Eq. (12) or Eq. (16) for the dication. From Table V, as compared with the For the PDM2-TDM2-TIC0 model, we see that TIC in the ion has no significant effect in the orientation-averaged dication yields. The orientation-dependent dication yields are almost identical between these two models. Influence of the TIC in the ion is weak because the TI rate to form dication is much faster than the rate of population transfer via laser couplings.

For the PDM2-TDM2-TIC2 model, we solve Eq. (6) with the ionization matrices in Eqs. (7)–(9). From Table V, we see that the $^1A_1$ population from PDM2-TDM2-TIC2 is about 30% larger than that from PDM2-TDM2-TIC0. However, population of the $^1B_1$ state is decreased by 22%. Influence of the TIC in the dication is more significant than in the ion because there are more time for laser couplings to take place.

Finally, we compare the angular distribution of the $^1A_1$, $^1B_1$, and the $^1A_2$ states obtained from PDM2-TDM2-TIC2 to those obtained from PDM2-TDM2-TIC0. From Fig. 7, we see that yield of the $^1A_1$ and $^1B_1$ states increases and decreases for $\gamma < 45°$ and $30° < \beta < 150°$, respectively, when TIC is included. This is opposite to what we observed in the previous subsection when comparing PDM2-TDM2-TIC0 to PDM2-TDM1-TIC0. Yield of the $^1A_2$ and $^1B_1$ state is now symmetric and asymmetric about $\beta = 90°$, which is also opposite to the PDM2-TDM2-TIC0 model results. These can be explained by the interplay of coherence and laser couplings.
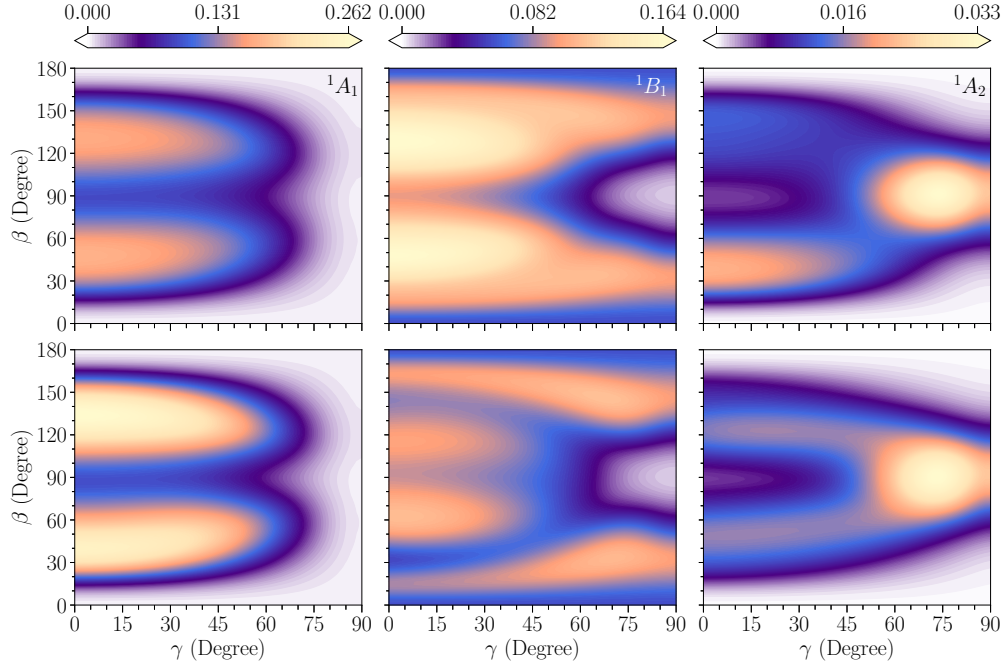
FIG. 7. Top row: Orientation-dependent dication yields for the $^1A_1$, $^1B_1$, and $^1A_2$ states, calculated using the `PDM2-TDM2-TIC0` model. Bottom row: Same yields but calculated using the `PDM2-TDM2-TIC2` model. All other states have very similar distributions and are not shown here. The tunnel ionization coherence in the dication states affects the laser couplings between these states, leading to the angular distributions in the bottom row.

From Eq. (6), evolution of the population is

$$\frac{d}{dt}\rho_{ii}^{(2)}(t) = -2\sum_{l}\vec{d}_{il}\cdot\vec{E}(t)\,\text{Im}\left[\rho_{li}^{(2)}(t)\right] + \Gamma_{ii}^{(2)}(t). \quad (17)$$

As TIC in the dication is included, the sign of $\rho_{li}^{(q)}(t)$ could be flipped at a certain time, causing the population transfer to happen in the opposite direction. We note that a change of sign in the TDMs or the phase in the structure parameters could produce similar effects based on Eq. (17). Since these conventions are rather arbitrary, one should be aware of the inherent uncertainty in the modeling, as similarly suggested by Ref. [49].

D. Effects of carrier envelope phase

The influence of tunnel ionization coherence in the dication raises concerns over the dependence of the orientation-averaged dication yields on the CEP of the laser pulse. This is because the CEP could also have an impact on the population transfer through Eq. (17). Consequently, if the laser pulses used in experiments are not CEP stabilized, then it could further increase the uncertainty in the measurements. Taking advantage of the computational efficiency of the DM-SDI model, we perform the calculations with CEPs ranging from $[-\pi, \pi]$ using the `PDM2-TDM2-TIC2` model.

Figure 8 displays the orientation-averaged dication yields calculated using `PDM2-TDM2-TIC2` with different CEPs. For convenience, we plot the results as the absolute value of the relative difference to the zero CEP results in percentage. We can see that all changes are below 5%, such that random CEPs should not introduce significant uncertainty to the observables. The maximum change occurs when the CEP is around

$\pi/4$ for the $^1A_2$ state (state 5), which could be formed from the B state (cf. Table I). As discussed in Sec. III B, the influence of the A-B coupling on the orientation-averaged dication yield
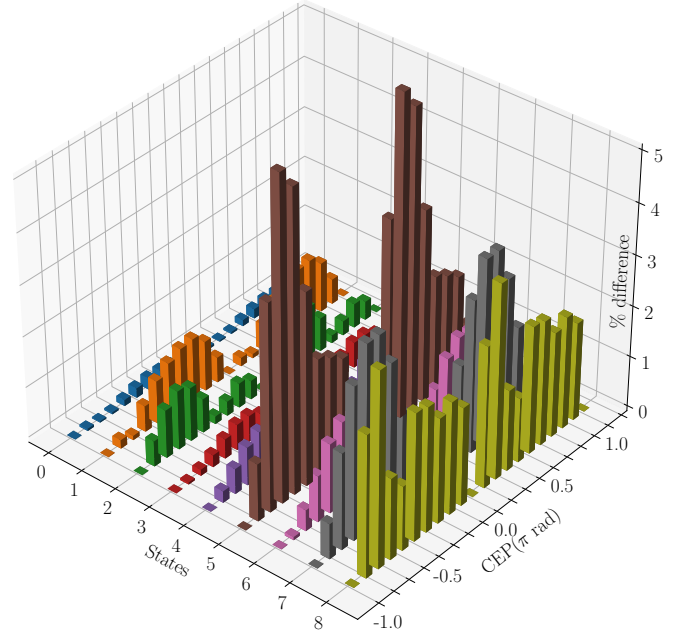

FIG. 8. Orientation-averaged dication yields calculated using `PDM2-TDM2-TIC2` with different CEP of the laser pulse. Results are presented as the relative difference (%) to the zero CEP results. The largest difference is less than 5%, such that influence of CEP on the averaged dication yields is insignificant.

is also around 5%. Therefore, if the CEP is not stabilized in pump-probe experiments for H_2O, then the A-B vibronic coherence is unlikely to be identified, while signatures of the X-A vibronic coherence should be still visible.

IV. CONCLUSION AND OUTLOOK

To conclude, we have extended the DM-SDI model from homonuclear diatomic molecules to general molecules with permanent dipole moments and arbitrary symmetry. Through the application of the theory to the water molecule, we found that the linear Stark shift could play a significant role in the SDI dynamics of polar molecule. The dipole couplings between the ionic states and between the dication states have also found to to be important. Meanwhile, the tunnel ionization coherence was found to have moderate influences on the dication yield.

By using different levels of theory, we identified the formation mechanisms for states 0–6 of H_2O^{2+}:

$^3B_1(0)$: Linear Stark shift enhanced tunnel ionization (LSS-ETI) and the X-A laser coupling (cf. Fig. 5).

$^1A_1(1)$, $^1B_1(2)$, $^1A_2(5)$: LSS-ETI, the X-A laser coupling, and the laser couplings with each other(cf. Figs. 6 and 7).

$^3A_2(3)$ and $2^1A_1(4)$: LSS-ETI (cf. Fig. 4).

$^3B_2(6)$: LSS-ETI and the laser coupling with the $^3A_2$ state (cf. Fig. 6).

Given the role played by the X-A laser coupling in the formation of states 0–2 and 5, we predict that signature of the X-A vibronic coherence could be observed in both two-body and three-body kinetic energy release spectra when SDI is used to probe charge migration in the water cation. We expect that permanent dipole moments of generic polar molecules will play a similar role as in the case of the water molecule because LSS-ETI is a general phenomenon. But the role of laser couplings between ionic states and dication states would be largely target dependent.

From the example of water SDI, we see that to determine whether SDI can probe vibronic coherence between some states, we do not need to know the details of the dissociation dynamics. What one needs to know *a priori* are which ionic states are populated predominantly by the pump laser and the electronic structures of those states, such as excitation energies and transition dipole moments. Since the formation pathway of some dication states always depends on the laser couplings between ionic states, experimental observables from SDI would always carry the signature of vibronic coherence between those ionic states. Knowing the physical origins of modulations in the observables, the effort to interpret the observables from the SDI probe can then be greatly simplified.

The validity of the current theory depends on the laser pulses used in the experiment. The main assumption of the theory is that nuclear motion can be regarded as frozen during the ionization process. Since pulse duration is limited to roughly one optical cycle, for pulse duration to be around 6 fs, the central wavelength of the laser pulses should be less than 1.8 μm. Another assumption of the theory is that the laser is intense enough to drive the tunneling ionization of the ion. Estimating the Kelydsh parameter to be $\gamma = \sqrt{I_p/2U_p} \sim 0.5$ and $I_p \sim 27.2$ eV for a typical ionization potential of a molecular ion, the pondermotive potential is then $U_p = F_0^2/4\omega^2 \sim 54.4$ eV. Therefore, for a 750 nm or 1 μm laser, the required peak laser intensity would then be around 1 or $0.6 \, PW/cm^2$. For lasers with a shorter wavelength, U_p could be too small such that adiabatic approximation for tunneling ionization may no longer be true.

Finally, advancements in nonlinear compression have showcased the ability to generate high-energy IR pulses (~ 1 μm wavelength) with pulse durations as short as approximately 3 fs [58]. If the prepulse and the postpulse of the single-cycle IR pulse can be well controlled, then the cross-correlation between the IR pump and probe could be shorter than using a single-cycle IR pump and a high-harmonic generated attosecond soft x-ray probe, leading to unprecedented time resolution for pump-probe study of vibronic coherence. This is because the wavelength of the driving laser for the soft x-ray pulse is typically longer. For example, 1.2- and 1.8-μm wavelength is needed to reach the carbon and nitrogen K edge, respectively. To ensure the pump and probe pulse are phase-locked for coherence spectroscopy, the longer-wavelength driving laser is used as the pump, resulting in longer cross-correlation than that of 1 μm IR pump probe. Therefore, single-cycle IR pump-probe experiments could hold exciting prospects for probing vibronic coherence in molecules.

[1] C. Guo, M. Li, J. P. Nibarger, and G. N. Gibson, Phys. Rev. A **58**, R4271 (1998).

[2] A. T. Eppink and D. H. Parker, Rev. Sci. Instrum. **68**, 3477 (1997).

[3] J. Ullrich, R. Moshammer, R. Dörner, O. Jagutzki, V. Mergel, H. Schmidt-Böcking, and L. Spielberger, J. Phys. B: At. Mol. Opt. Phys. **30**, 2917 (1997).

[4] J. Ullrich, R. Moshammer, A. Dorn, R. Dörner, L. P. H. Schmidt, and H. Schmidt-Böcking, Rep. Prog. Phys. **66**, 1463 (2003).

[5] S. Voss, A. S. Alnaser, X. M. Tong, C. Maharjan, P. Ranitovic, B. Ulrich, B. Shan, Z. Chang, C. D. Lin, and C. L. Cocke, J. Phys. B: At. Mol. Opt. Phys. **37**, 4239 (2004).

[6] A. S. Alnaser, S. Voss, X.-M. Tong, C. M. Maharjan, P. Ranitovic, T. Osipov, B. Shan, Z. Chang, and C. L. Cocke, Phys. Rev. Lett. **93**, 113003 (2004).

[7] C. Wu, Y. Yang, Z. Wu, B. Chen, H. Dong, X. Liu, Y. Deng, H. Liu, Y. Liu, and Q. Gong, Phys. Chem. Chem. Phys. **13**, 18398 (2011).

[8] S. De, I. A. Bocharova, M. Magrakvelidze, D. Ray, W. Cao, B. Bergues, U. Thumm, M. F. Kling, I. V. Litvinyuk, and C. L. Cocke, Phys. Rev. A **82**, 013408 (2010).

[9] S. De, M. Magrakvelidze, I. A. Bocharova, D. Ray, W. Cao, I. Znakovskaya, H. Li, Z. Wang, G. Laurent, U. Thumm, M. F. Kling, I. V. Litvinyuk, I. Ben-Itzhak, and C. L. Cocke, Phys. Rev. A **84**, 043410 (2011).

[10] X. Xie, K. Doblhoff-Dier, H. Xu, S. Roither, M. S. Schöffler, D. Kartashov, S. Erattupuzha, T. Rathje, G. G. Paulus, K. Yamanouchi, A. Baltuska, S. Grafe, and M. Kitzler, Phys. Rev. Lett. **112**, 163003 (2014).

[11] S. Zhao, B. Jochim, P. Feizollah, J. Rajput, F. Ziaee, P. KanakaRaju, B. Kaderiya, K. Borne, Y. Malakar, B. Berry, J. Harrington, D. Rolles, A. Rudenko, K. D. Carnes, E. Wells, I. Ben-Itzhak, and T. Severt, Phys. Rev. A **99**, 053412 (2019).

[12] N. Iwamoto, C. J. Schwartz, B. Jochim, K. Raju P, P. Feizollah, J. Napierala, T. Severt, S. Tegegn, A. Solomon, S. Zhao, H. Lam, T. N. Wangjam, V. Kumarappan, K. D. Carnes, I. Ben-Itzhak, and E. Wells, J. Chem. Phys. **152**, 054302 (2020).

[13] T. Townsend, C. J. Schwartz, B. Jochim, T. Severt, N. Iwamoto, J. L. Napierala, P. Feizollah, S. N. Tegegn, A. Solomon, S. Zhao, K. D. Carnes, I. Ben-Itzhak, and E. Wells, Front. Phys. **9**, 691727 (2021).

[14] G. Basnayake, P. Hoerner, B. Mignolet, M. K. Lee, Y. F. Lin, A. H. Winney, D. A. Debrah, L. Popaj, X. Shi, S. K. Lee, H. Bernhard Schlegel, F. Remacle, and W. Li, Phys. Chem. Chem. Phys. **23**, 23537 (2021).

[15] T. Severt, D. R. Daugaard, T. Townsend, F. Ziaee, K. Borne, S. Bhattacharyya, K. D. Carnes, D. Rolles, A. Rudenko, E. Wells, and I. Ben-Itzhak, Phys. Rev. A **105**, 053112 (2022).

[16] A. J. Howard, C. Cheng, R. Forbes, G. A. McCracken, W. H. Mills, V. Makhija, M. Spanner, T. Weinacht, and P. H. Bucksbaum, Phys. Rev. A **103**, 043120 (2021).

[17] C. Cheng, Z. L. Streeter, A. J. Howard, M. Spanner, R. R. Lucchese, C. W. McCurdy, T. Weinacht, P. H. Bucksbaum, and R. Forbes, Phys. Rev. A **104**, 023108 (2021).

[18] A. J. Howard, M. Britton, Z. L. Streeter, C. Cheng, R. Forbes, J. L. Reynolds, F. Allum, G. A. McCracken, I. Gabalski, R. R. Lucchese, C. W. McCurdy, T. Weinacht, and P. H. Bucksbaum, Commun. Chem. **6**, 81 (2023).

[19] L. S. Cederbaum and J. Zobeley, Chem. Phys. Lett. **307**, 205 (1999).

[20] A. S. Folorunso, A. Bruner, F. Mauger, K. A. Hamer, S. Hernandez, R. R. Jones, L. F. DiMauro, M. B. Gaarde, K. J. Schafer, and K. Lopata, Phys. Rev. Lett. **126**, 133002 (2021).

[21] Y. Kobayashi, D. M. Neumark, and S. R. Leone, Phys. Rev. A **102**, 051102(R) (2020).

[22] Y. Kobayashi, K. F. Chang, S. M. Poullain, V. Scutelnic, T. Zeng, D. M. Neumark, and S. R. Leone, Phys. Rev. A **101**, 063414 (2020).

[23] D. T. Matselyukh, V. Despré, N. V. Golubev, A. I. Kuleff, and H. J. Wörner, Nat. Phys. **18**, 1206 (2022).

[24] F. Remacle, R. Levine, and M. Ratner, Chem. Phys. Lett. **285**, 25 (1998).

[25] F. Remacle and R. D. Levine, Proc. Natl. Acad. Sci. USA **103**, 6793 (2006).

[26] F. Lépine, M. Y. Ivanov, and M. J. Vrakking, Nat. Photon. **8**, 195 (2014).

[27] C. H. Yuen and C. D. Lin, Phys. Rev. A **106**, 023120 (2022).

[28] C. H. Yuen, P. Modak, Y. Song, S.-F. Zhao, and C. D. Lin, Phys. Rev. A **107**, 013112 (2023).

[29] C. H. Yuen and C. D. Lin, Phys. Rev. A **109**, L011101 (2024).

[30] S. Mukamel, *Principles of Nonlinear Optical Spectroscopy*, Oxford Series in Optical and Imaging Sciences (Oxford University Press, Oxford, 1995).

[31] V. May and O. Kühn, *Charge and Energy Transfer Dynamics in Molecular Systems* (John Wiley & Sons, New York, 2023).

[32] N. Rohringer and R. Santra, Phys. Rev. A **79**, 053402 (2009).

[33] R. Santra, V. S. Yakovlev, T. Pfeifer, and Z.-H. Loh, Phys. Rev. A **83**, 033405 (2011).

[34] S. G. S. Adrian N. Pfeiffer and S. R. Leone, Mol. Phys. **111**, 2283 (2013).

[35] Q. Zhang, H. Xie, G. Li, X. Wang, H. Lei, J. Zhao, Z. Chen, J. Yao, Y. Cheng, and Z. Zhao, Commun. Phys. **3**, 1 (2020).

[36] C. H. Yuen and C. D. Lin, Phys. Rev. A **108**, 023123 (2023).

[37] Z. Wu, C. Wu, X. Liu, Y. Liu, Y. Deng, and Q. Gong, Opt. Express **18**, 10395 (2010).

[38] G. A. McCracken, A. Kaldun, C. Liekhus-Schmaltz, and P. H. Bucksbaum, J. Chem. Phys. **147**, 124308 (2017).

[39] G. A. McCracken and P. H. Bucksbaum, J. Chem. Phys. **152**, 134308 (2020).

[40] C. Cheng, R. Forbes, A. J. Howard, M. Spanner, P. H. Bucksbaum, and T. Weinacht, Phys. Rev. A **102**, 052813 (2020).

[41] S. Petretti, A. Saenz, A. Castro, and P. Decleva, Chem. Phys. **414**, 45 (2013),.

[42] L. B. Madsen, F. Jensen, O. I. Tolstikhin, and T. Morishita, Phys. Rev. A **89**, 033412 (2014).

[43] J. Benda, J. D. Gorfinkiel, Z. Mašín, G. S. J. Armstrong, A. C. Brown, D. D. A. Clarke, H. W. van der Hart, and J. Wragg, Phys. Rev. A **102**, 052826 (2020).

[44] Z. L. Streeter, F. L. Yip, R. R. Lucchese, B. Gervais, T. N. Rescigno, and C. W. McCurdy, Phys. Rev. A **98**, 053429 (2018).

[45] D. Reedy, J. B. Williams, B. Gaire, A. Gatton, M. Weller, A. Menssen, T. Bauer, K. Henrichs, P. Burzynski, B. Berry, Z. L. Streeter, J. Sartor, I. Ben-Itzhak, T. Jahnke, R. Dörner, T. Weber, and A. L. Landers, Phys. Rev. A **98**, 053430 (2018).

[46] S.-F. Zhao, J. Xu, C. Jin, A.-T. Le, and C. D. Lin, J. Phys. B: At. Mol. Opt. Phys. **44**, 035601 (2011).

[47] O. I. Tolstikhin, T. Morishita, and L. B. Madsen, Phys. Rev. A **84**, 053423 (2011).

[48] M. A. Morrison and G. A. Parker, Aust. J. Phys. **40**, 465 (1987).

[49] G. Yuan, S. Jiang, Z. Wang, W. Hua, C. Yu, C. Jin, and R. Lu, Struct. Dyn. **6**, 054102 (2019).

[50] X.-M. Tong, Z. X. Zhao, and C.-D. Lin, Phys. Rev. A **66**, 033402 (2002).

[51] D. A. Varshalovich, A. N. Moskalev, and V. K. Khersonskii, *Quantum Theory of Angular Momentum* (World Scientific, Singapore, 1988).

[52] B. Gervais, E. Giglio, L. Adoui, A. Cassimi, D. Duflot, and M. E. Galassi, J. Chem. Phys. **131**, 024302 (2009).

[53] I. Fdez. Galván, M. Vacher, A. Alavi, C. Angeli, F. Aquilante, J. Autschbach, J. J. Bao, S. I. Bokarev, N. A. Bogdanov, R. K. Carlson, L. F. Chibotaru, J. Creutzberg, N. Dattani, M. G.

Delcey, S. S. Dong, A. Dreuw, L. Freitag, L. M. Frutos, L. Gagliardi, F. Gendron *et al.*, J. Chem. Theory Comput. **15**, 5925 (2019).

[54] C. Ning, B. Hajgató, Y. Huang, S. Zhang, K. Liu, Z. Luo, S. Knippenberg, J. Deng, and M. Deleuze, Chem. Phys. **343**, 19 (2008).

[55] N. Tancogne-Dejean, M. J. T. Oliveira, X. Andrade, H. Appel, C. H. Borca, G. Le Breton, F. Buchholz, A. Castro, S. Corni, A. A. Correa, U. De Giovannini, A. Delgado, F. G. Eich,

J. Flick, G. Gil, A. Gomez, N. Helbig, H. Hübener, R. Jestädt, J. Jornet-Somoza *et al.*, J. Chem. Phys. **152**, 124119 (2020).

[56] X. Andrade and A. Aspuru-Guzik, Phys. Rev. Lett. **107**, 183002 (2011).

[57] V.-H. Hoang, S.-F. Zhao, V.-H. Le, and A.-T. Le, Phys. Rev. A **95**, 023407 (2017).

[58] M.-S. Tsai, A.-Y. Liang, C.-L. Tsai, P.-W. Lai, M.-W. Lin, and M.-C. Chen, Sci. Adv. **8**, eabo1945 (2022).